



Visible-light-induced reduction of Cr(VI) by PDPB-ZnO nanohybrids and its photo-electrochemical response

Srabanti Ghosh^{a,*}, Hynd Remita^{b,c}, Rajendra N. Basu^a

^a Fuel Cell & Battery division, CSIR-Central Glass and Ceramic Research Institute, 196, Raja S.C. Mullick Road, Kolkata-, 700032, India

^b Laboratoire de Chimie Physique, UMR 8000-CNRS, Université Paris-Sud, Université Paris Saclay, 91405 Orsay, France

^c CNRS, Laboratoire de Chimie Physique, UMR 8000, 91405 Orsay, France



ARTICLE INFO

Keywords:

Poly(diphenylbutadiyne) nanofibers
ZnO nanoparticles
Photocatalysis
Cr (VI) removal
Photoelectrochemical properties

ABSTRACT

Photochemical conversion of solar photons is one of the most promising solutions to produce usable forms of energy such as electricity, solar fuels and environmental remediation. We have developed an efficient visible light active poly(diphenylbutadiyne) (PDPB)-ZnO nanohybrids (NHS) by facile adsorption of ZnO nanoparticles on PDPB nanofibers. The as-prepared PDPB-ZnO NHS demonstrated enhanced photocatalytic activity compared to bare PDPB for the photoreduction of hexavalent chromium Cr(VI). Among the hybrid photocatalysts, PDPB-ZnO with 10 wt% of PDPB exhibited highest catalytic activity for Cr(VI) reduction under visible light irradiation. X-ray photoelectron spectroscopy data revealed the presence of Cr(III) on the surface of nanohybrid during photo-reduction of Cr(VI). The enhanced photocatalytic activity of nanohybrids could be attributed from the co-sensitization of ZnO NPs by oligomeric and polymer chain unit of PDPB nanofibers and efficient separation of photogenerated charge carriers as followed by impedance analysis and photocurrent measurements. PDPB-ZnO NHS showed enhanced photoelectrochemical current density by a factor of ~8.1 compared to bare PDPB nanofibers and long-term stability under longer visible light illumination. The Mott–Schottky plot revealed that photo generated charge carrier concentration has been increased for PDPB-ZnO NHS ($8.5 \times 10^{19} \text{ cm}^{-3}$) compare to pure ZnO ($2.5 \times 10^{19} \text{ cm}^{-3}$). The present study provide an effective approach for the development of organic-inorganic nanohybrids which are suitable for photocatalytic removal of heavy metal ions as well as photoelectrochemical response revealing water splitting that would be useful in designing future solar devices.

1. Introduction

Light-driven chemical transformations offer an attractive and sustainable solution for clean energy production and environmental remediation through water splitting and toxic organic molecule degradation [1–4]. Consequently, a rapid progress has been made to develop visible-light-sensitive materials for photocatalysis as visible light hold energy up to 43% of total sun energy and understanding how to maximize solar light harvesting [5–7]. Accordingly, photocatalysis technology has proven to be a useful strategy for removing heavy metal pollution, particularly hexavalent chromium Cr(VI), exist in wastewater by various industrial processes such as leather tanning, electroplating, pigment and paint manufacturing, textile production, steel fabrication etc. Notably, Cr(VI) is highly toxic to the microorganisms and potentially harmful to human health due to genotoxic effects such as chromosomal aberrations, gastrointestinal disorders, haemorrhagic diaisis and lung cancer etc [8–11]. Conventionally, heterogeneous

catalysis has relied upon titanium dioxide (TiO_2) or zinc oxides (ZnO) based semiconductor oxides, widely used photocatalytic materials for the removal of environmental pollutants under UV light [12–16]. In order to improve the catalytic activity of semiconductor materials under visible light region, various method including metal ion doping, carbon doping, and hydrogenation usually followed at elevated temperature or high pressure [17–22]. Hence, designing of new materials for sustainable energy applications is one of the important issues in material science. Other semiconductor and composites based visible light active photocatalysts such as SnS_2 [23,24], $\text{Cu}_2\text{ZnSnS}_4$ [25], carbon nanofiber/ SnS_2 [26], PANI/ $\text{MnO}_2/\text{TiO}_2$ [27], $\alpha\text{-MnO}_2@\text{RGO}$ [28], $\text{Fe}_3\text{O}_4/\text{RGO}$ [29] and phthalocyanine modified TiO_2 [30] have been reported for the reduction of Cr(VI) to Cr(III).

Recently, metal free organic semiconductors, conjugated polymer nanostructures emerged as novel visible light-driven photocatalysts for pollutant degradation [31–35]. It has been shown that poly-diphenylbutadiyne (PDPB) nanofibers exhibited a narrow band gap of

* Corresponding author.

E-mail address: rnbasu@cgcri.res.in (S. Ghosh).

about 1.68 eV and absorbed visible light up to 800 nm [32]. These nanofibers were very active for degradation of organic pollutants under visible light. Moreover, very high catalytic activity was also achieved by using another conducting polymer, poly(3,4-ethylenedioxithiophene) (PEDOT) nanospindle for photodegradation of organic contaminants under visible light [33]. Floresyona et al. [34] developed poly (3-hexylthiophene) (P3HT) nanostructures which can easily be deposited on flat quartz supports for photocatalytic degradation of organic pollutants (phenol and rhodamine B) under visible light with highly accelerated degradation kinetics, which opens new perspectives in photocatalytic reactors without the need of a separation step by centrifugation and also find application in self-cleaning surfaces. Recently, a series of porous conjugated polymers also demonstrated superior catalytic activity for hydrogen production under visible light [36–38]. However, the photocatalytic efficiency of semiconductors and particularly for pure conjugated polymer nanostructures is limited by the high recombination rate of its photogenerated charge carriers [39]. One way to improve solar light harvesting efficiency is coupling a semiconductor of large band gap with another semiconductor material of smaller band gap which allows broadening of solar light absorption range with enhanced photo generated charge separation, thus considerably improve the catalytic activity [40,41]. Very recently, Ghosh et al. reported that the amalgamation of plasmonic nanocrystals into conjugated polymers can improve charge separation as well as useful to promote photocatalysis under visible light where metallic nanostructures act as the light absorber and also increases catalytic active site [42]. Few studies have been conducted using PDPB nanofibers as component for synthesizing semiconductor based composites with high catalytic activity [43,44]. In this regards, Ghosh and co-workers studied the ultrafast photoinduced charge separation at the semiconductor-conducting polymer heterojunction (ZnO-PDPB) interface which is suitable for efficient solar light harvesting [45]. However, successful and wide catalytic application of these materials relies significantly on robust NPs engineering and have not been well explored yet.

In this paper, PDPB-ZnO nanohybrid based catalysts with different weight ratios of PDPB nanofibers with ZnO NPs were synthesized via a solution phase synthetic route. After modification of ZnO with polymer chain unit of PDPB nanofibers showed visible light induced photo-reduction of toxic Cr(VI) to Cr(III) and photoelectrochemical water splitting.

2. Experimental section

2.1. Reagents

Analytical grade chemicals, such as sodium dodecyl sulfate (SDS), sodium chloride, cyclohexane (> 99%), pentanol ($\geq 99\%$), ZnO (~ 30 nm) and potassium dichromate were purchased from Sigma-Aldrich, USA. For *in-situ* polymerization, 1, 4-diphenylbutadiyne (DPB) (Aldrich) and benzoin methyl ether (BME) (Fluka) used as received without further purifications. Ultrapure water (Millipore System, 18.2 M Ω cm) and ethanol ($\geq 99\%$) were used as solvents.

2.2. Synthesis of polymer nanostructures

Swollen hexagonal mesophases were used as soft template for preparation of the polymer nanostructures following the previous method with some modifications [32,46]. Typically, 1 g of sodium dodecyl sulfate was dissolved in 2 mL of 0.3 mol.L $^{-1}$ NaCl. After obtaining a transparent and viscous micellar solution through vigorous stirring, cyclohexane containing 1, 4-diphenylbutadiyne (DPB) monomer (10% of mass) and initiator benzoin methyl ether (BME) (1%) was mixed in the micellar solution under stirring leads to a white unstable emulsion. A co-surfactant, pentanol-1 (420 μ L) was then added to the mixture and after vigorous stirring, a translucent, birefringent and stable gel was obtained which yielded a hexagonal mesophase. In order to synthesize

polymer nanostructures, the doped mesophases were irradiated by light with an Oriel 300 W Xenon UV-vis lamp at a distance of 5 cm for 12 h. After reaction, the material was extracted in a water-ethanol mixture, centrifuged, and washed several times to completely remove the surfactant.

2.3. Preparation of PDPB-ZnO nanohybrids (NHs)

PDPB-ZnO NHs were prepared by dispersing ZnO nanoparticles into the ethanolic solution of as prepared PDPB nanofibers (1%, 4%, 10%, 20% and 50%). The solutions were stirred for 48 h in the dark and then separated by centrifugation. The as-prepared yellowish powder was then dried in an oven at 50 °C and stored in the dark.

2.4. Characterization methods

Transmission electron microscopy (TEM) was carried out using an FEI (Technai S-Twin) instrument with acceleration voltage of 200 kV. Field emission scanning electron microscopy (FESEM, QUANTA FEG 250) was used to investigate the surface morphology of the samples. X-ray powder diffractogram (XRD) was recorded in the 20 range 10°–80° at a slow scanning rate of 1° min $^{-1}$ by an X-ray Diffractometer (Philips X'Pert, The Netherlands) with Cu K α radiation (at 40 kV and 40 mA). The steady-state absorption was determined with a Shimadzu UV-2450 spectrophotometer. Thermogravimetric analysis (TGA) of the powder sample of PDPB and PDPB-ZnO have been carried out under argon flow at a heating rate of 10 °C min $^{-1}$ using a simultaneous thermal analyzer (STA 449 F, Netzsch, Germany). Brunauer–Emmett–Teller (BET) surface area measurements were carried out by nitrogen gas adsorption at 77.3 K using a Quantachrome (USA) Autosorb surface analyzer. The samples were degassed under vacuum at 120 °C for 3 h prior to measurement. Pore size distribution was calculated from desorption isotherm by the Barrett–Joyner–Halenda (BJH) method. For XPS study, ZnO and PDPB-ZnO samples were prepared in pallet form and the analysis was carried out in a PHI 5000 VersaProbe II spectrophotometer (Physical Electronics Inc., USA) using a monochromatized Al K α (~ 1486.6 eV) X-ray beam of size ~ 100 μ m. Prior to XPS analysis, sample surfaces were sputtered with a 2 kV rastered Ar $^{+}$ ion beam for one minute to clean the surface. During XPS measurements, dual beam charge neutralization system was operated in order to neutralize the generated static charges on the sample surface. Recorded high resolution C 1s photoelectron spectra were resolved into their respective Gaussian fits after removal of background intensity. The photoluminescence (PL) spectrum of as synthesized materials was taken by JASCO FP-8500. Fourier transformed infrared spectra (FTIR) of ZnO, PDPB, and PDPB-ZnO was recorded using a JASCO FTIR-6300 spectrometer. Scanning wavelengths were varied from 4000–600 with a 2 cm $^{-1}$ spectral resolution with 100 repetitions scans average for each spectrum. The photoresponse of ZnO, PDPB, and PDPB-ZnO was measured under periodic chopped irradiation from Xe-arc lamp (100 W) as a white-light source with an incident beam intensity of 100 mW/cm 2 .

2.5. Photocatalytic tests

The photocatalytic activity of the PDPB, PDPB-ZnO NHs and physical mixture of PDPB and ZnO under visible light illumination has been tested for photoreduction of Cr (VI) in water. The photoreduction of Cr (initial concentration $C_0 = 10, 20, 50, 100, 200, 300$ mg/L) was carried out in an quartz cell reactor containing 50 mL of a Cr (VI) solution with a concentration of 0.5 g.L $^{-1}$ of the PDPB-ZnO. For control experiment, the PDPB nanofiber (0.5 g.L $^{-1}$) and ZnO NPs (0.5 g.L $^{-1}$) have been studied separately. The suspension was irradiated with a mercury lamp, $\lambda \geq 450$ nm (under UV-vis light) and appropriate amount of aliquots were collected from the reactor at successive time intervals. The percentage reduction (%RE) of Cr (VI) was determined using Equation 1:

$$\%RE = \frac{I_0 - I}{I_0} \times 100 \quad (1)$$

where, I_0 is the initial absorption intensity of Cr (VI) at $\lambda_{\text{max}} = 460$ nm and I is the absorption intensity after solar light irradiation.

2.6. Photoelectrochemical response

Cyclic voltammetry measurements were performed by using a galvanostat – potentiostat (PGSTAT 30, Autolab, The Netherlands) electrochemical workstation at a scanning rate of 50 mVs^{-1} with a standard three-electrode electrolytic cell. A Pt foil used as the counter electrode. All potentials were reported against the Ag/AgCl reference electrode. Prior to performing the measurements, the electrolyte solution was purged with high-purity nitrogen gas for at least 30 min. The glassy carbon electrode (GCE) was used as working electrode. For electrode preparation, the surface of a GCE was polished with 1.0, 0.3 and $0.05 \mu\text{m}$ α -alumina powders in sequence, rinsed thoroughly with twice distilled water and placed in a water-filled ultrasonic bath over a 2 min period. After dried in air, the nanostructured catalysts were deposited on the surface of GCE for electrochemical measurement. The transient photocurrent responses and Mott–Schottky plot of the samples were determined using above electrochemical working station. Linear sweep voltammetry scans were measured under dark and visible light illumination from a 250 W xenon lamp fitted with a filter that cuts light with wavelengths ≥ 450 nm and output illumination intensity of 100 mW cm^{-2} . Chronoamperometric measurement was carried out to check the stability of the catalytic material under visible light irradiation. The electrochemical impedance measurements were carried out using the same experimental setup as mentioned earlier with the help of Autolab-30, PG-Stat FRA-II (software NOVA 1.10, Metrohm, The Netherlands). The Nyquist plots were taken at an applied potential of 0.4 V vs. RHE and 100 kHz frequency using ac RMS amplitude of 10 mV.

3. Results and discussion

3.1. Synthesis of polymer and nanohybrids

For the fabrication of polymer based nanohybrids (NHs), hexagonal mesophases has been used as a soft template for the controlled synthesis of PDPB nanofibers under UV irradiation [33,46]. The oil domain of the mesophases is doped with 1, 4-diphenylbutadiyne monomers, which can directly polymerize by photo-irradiation in the presence of a free-radical initiator (benzoin methyl ether) [46]. After extraction of polymer nanofibers from template, PDPB-ZnO NHs were synthesized via facile adsorption of ZnO NPs on polymer nanofibers (Scheme 1) [45].

3.2. Microstructures

Fig. 1a, b shows the SEM and TEM images of PDPB nanofibers with average diameter of 22 nm and few micron lengths. While, Fig. 1c, d indicates ZnO nanoparticles (20 nm) were loaded onto the PDPB nanofibers as evident from electron microscopy. HRTEM image of PDPB-ZnO NHs shows crystalline nature of ZnO NPs having the lattice fringes and the interplanar distances of ~ 0.26 nm corresponding to the spacing between two (002) planes of ZnO.

In order to check the chemical composition of the NHs, the as-prepared PDPB-ZnO NHs was analyzed by energy dispersive spectroscopy (EDS) with the help of STEM. The high-angle annular dark-field scanning TEM (HAADF-STEM) image suggested that the ZnO NPs distributed on polymer nanofibers with little aggregated structures as shown in Fig. S1a. Energy dispersive X-ray (EDS) analysis further confirmed the presence of C, O, and Zn elements in the hybrid nanomaterials and the corresponding elemental mapping results showed that all the elements were distributed homogeneously on the PDPB polymer (Fig. S1b, c and d). Hence, elemental mapping suggests that the

nanofibers supported nanoparticles are made of ZnO NPs. Moreover, the energy-disperse X-ray spectrum also illustrates the chemical composition of nanohybrid with the presence of C, Zn, O (Fig. S1e).

3.3. Phase purity and crystal structure

The successful formation of nanohybrids has been established by XRD. Fig. 2a displays XRD patterns of pure PDPB nanofibers, PDPB-ZnO NHs and ZnO NPs. The well-defined sharp peaks of ZnO can be indexed as the (100), (002), (101), (102), (110), (103), (200), (112) and (201) diffraction planes of wurtzite structure (JCPDS card number: 36–1451) [45]. The broad peak obtained in the XRD pattern of PDPB nanofibers due to diffraction from polymeric chains. The 10 wt % of PDPB-ZnO NHs shows a coexistence of both PDPB and ZnO phase. However, the broad peak from the PDPB nanofibers is not identified within the nanohybrid at very low loading of polymer up to 4 wt% (Supplementary, Fig. S2). No other crystal phases were obtained in the XRD patterns suggests purity of as-prepared nanohybrids. Moreover, the loading of polymer PDPB mass of as low as 4% and 10% have been determined from thermogravimetric analysis (Supplementary, Fig. S3).

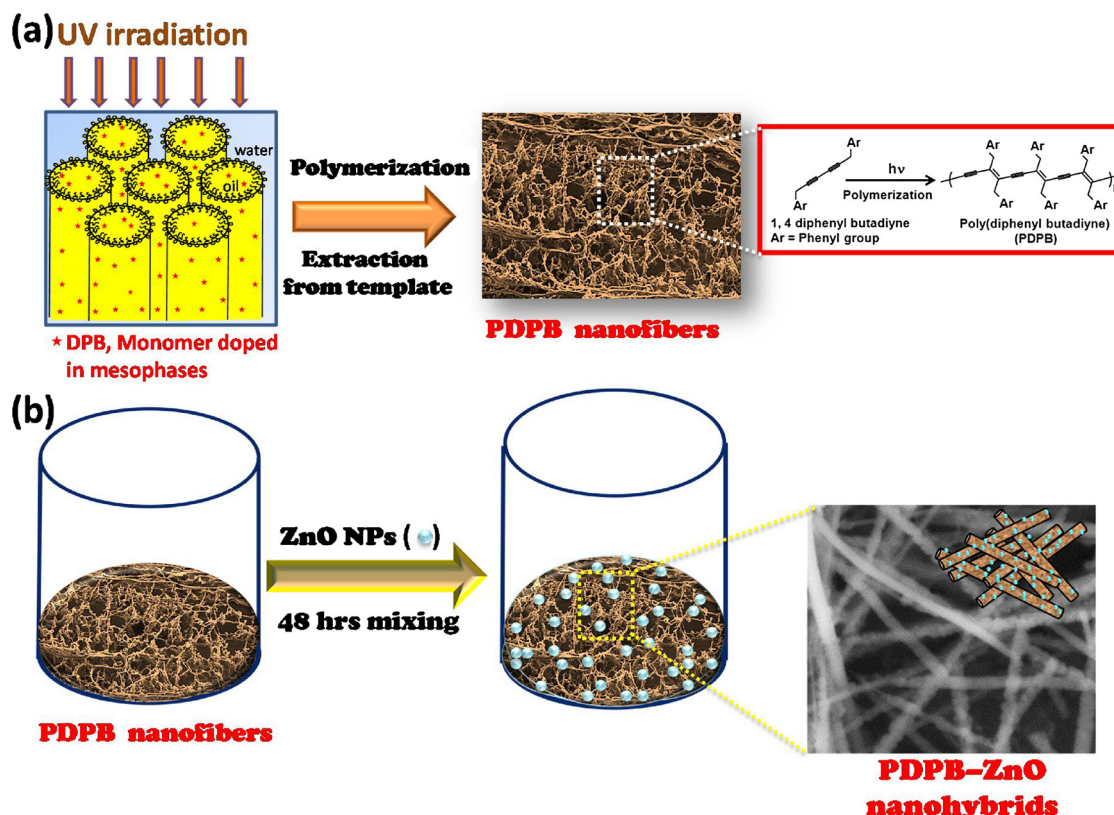
3.4. FTIR spectroscopy and chemical binding

The presence of PDPB polymer at the surface of ZnO NPs was followed by FTIR (Fig. 3).

The IR spectrum of ZnO usually shows a characteristic absorption band of Zn–O peak at 526 cm^{-1} and the other the peaks at 1586 and 1395 cm^{-1} are due to symmetric and asymmetric stretching vibration of C=O group of acetate suggesting presence of acetate anionic moieties at ZnO surface [47]. An additional weak broad peak around 3385 cm^{-1} is due to O–H stretching vibration. For PDPB, peaks at 2845 and 2923 cm^{-1} due to the symmetrical and asymmetrical stretching modes of the C–H bond respectively and other bands observed at 683 and 754 cm^{-1} are associated with the benzene ring out-of-plane deformations surface [45,46]. Moreover, the peaks in the 1400 to 1600 cm^{-1} region have been associated to the formation of the pi conjugated enyne unit which is overlapped with the spectrum region for aromatic ring stretching and bending mode. The large intensity change of C–H stretching modes has been attributed with frequencies in the range of 3100 – 3000 cm^{-1} . Particularly, the characteristic peak of pure PDPB at 3054 cm^{-1} corresponds to the C–H vibration involving hydrogen atoms in the para and meta positions get shifted to the high wave number (3060 cm^{-1}) and also become wider in PDPB-ZnO (10%) [45]. With further increase of polymer loading (up to 20%), the intensity of peak at 3065 and 2923 cm^{-1} is slightly enhanced which may suggests that the ZnO NPs are well integrated into the PDPB nanofibers.

3.5. X-ray photoelectron spectroscopy and surface compositions

To investigate the surface composition of the as-prepared PDPB-ZnO (10 wt %) NHs, X-ray photoelectron spectroscopy (XPS) was carried out. Fig. 4a shows the typical XPS wide survey spectra of pure ZnO NPs and PDPB-ZnO NHs. The C, Zn, and O peaks confirmed the presence of these elements in the NHs and the detected carbon is related to the presence of PDPB within the NHs. The Zn 2p consists of two peaks positioned at 1021.0 and 1044.2 eV for Zn $2p_{3/2}$ and Zn $2p_{1/2}$ (Fig. 4b), which have been observed in PDPB-ZnO NHs [48]. This suggests that the Zn exists in the Zn^{+2} state in both the ZnO and PDPB-ZnO NHs. The binding energy difference between the Zn $2p_{1/2}$ and Zn $2p_{3/2}$ is 23 eV which is well consistent with the literature report [49]. The O 1s can be deconvoluted by two nearly Gaussian curves for PDPB-ZnO NHs as shown in Fig. 4c. The binding energy components of 529.8 and 531.1 eV are attributed to O^{2-} ions in the Zn–O bonding of the wurtzite structure of ZnO [50] and the other peak is related to OH group absorbed onto the surface of the ZnO NPs respectively [51]. Fitting of C1s spectrum shows two peaks at 284.6 eV and 285.2 eV originating from



Scheme 1. Schematic diagram for the colloidal synthesis of (a) PDPB polymer nanofibers and (b) PDPB-ZnO nanohybrids.

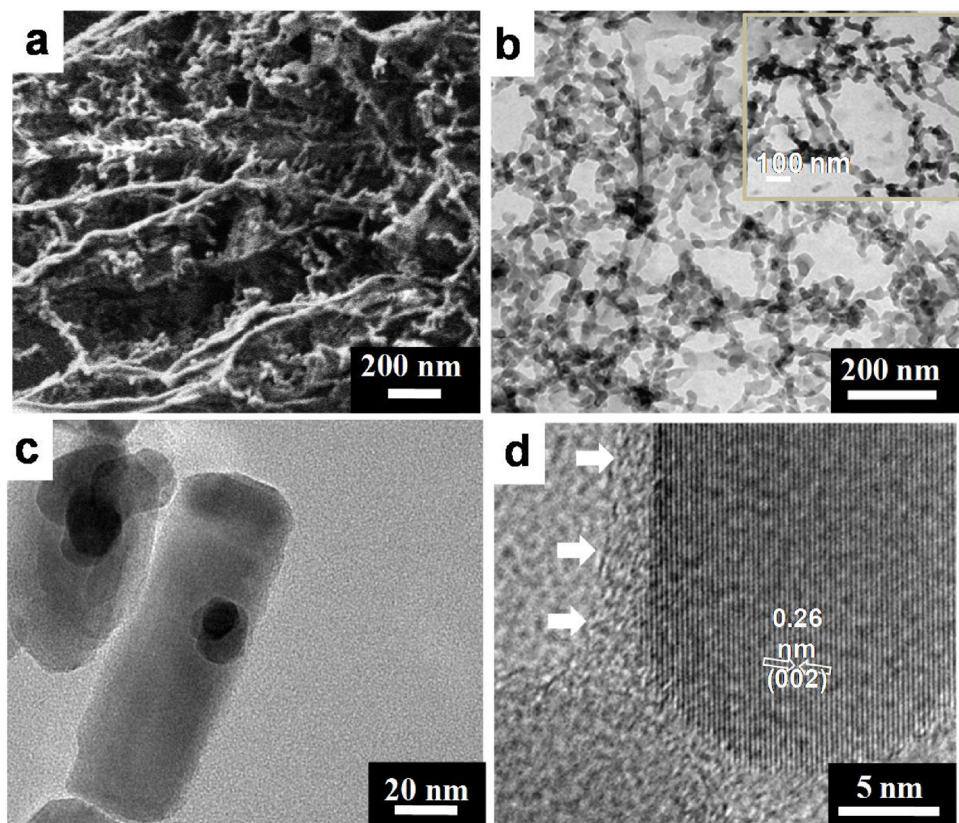


Fig. 1. Microscopic images of PDPB nanofibers and PDPB-ZnO nanohybrids (NHs). (a) SEM image and (b) TEM image of PDPB nanofibers. (c) TEM and (d) HRTEM images of PDPB-ZnO NHs. Polymeric zone marked with white arrow within the PDPB-ZnO NHs.

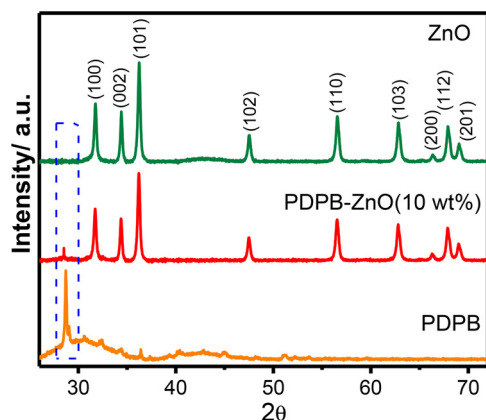


Fig. 2. X-ray diffraction patterns of PDPB (orange), PDPB-ZnO (red, 10 wt %) and ZnO (green). (For interpretation of the references to colour in this figure legend, the reader is referred to the web version of this article.)

the adventitious hydrocarbon from XPS instruments itself and C–C bond, respectively (Fig. 4d). Since PDPB polymers are made of carbon atoms, the C–C bond can be attributed to the carbon atoms which show a typical XPS spectrum of the carbon 1S centered at 285.0 eV [52].

3.6. UV-Vis spectroscopy

Fig. 5 displays UV-vis absorption spectra of pure ZnO, PDPB and PDPB-ZnO nanostructures. Pure ZnO NPs shows an absorption edge at about 365 nm, corresponding to the band-gap excitation ($E_g = 3.39$ eV) whereas the PDPB nanofibers has a broader absorption in the visible

range. From the cyclic voltammetry measurement, the estimated band gap for a PDPB was found to be 1.86 eV which is remarkably narrow and well consistent with the theoretically calculated band gap (1.95 eV) using density functional theory [33]. The PDPB-ZnO NHs demonstrates the characteristics of both PDPB and ZnO, and exhibits enhanced absorption in the visible range. With increasing the loading of PDPB, enhanced absorption in the visible region observed upto 1–10 wt% of PDPB, however, further increase in the loading of PDPB (20%), no significant enhancement has been observed in absorption spectra (Supplementary, Fig. S4). This indicates that PDPB-ZnO could be suitable for visible light harvesting for catalytic applications.

A type IV nitrogen adsorption-desorption isotherms can be observed for PDPB-ZnO NHs which confirms the mesoporosity of as-prepared nanohybrids (Supplementary, Fig. S5a). The Brunauer–Emmett–Teller (BET) surface area measurement reveals that the NHs have surface area of $24. m^2 g^{-1}$ with a broad size distribution in the range of 3–25 nm having an average pore size of ~7 nm and pore volume of $0.022 \text{ cm}^3 \text{ g}^{-1} \text{ nm}^{-1}$ (Supplementary, Fig. S5b).

3.7. Photocatalytic chromium removal

The photocatalytic activity of the as-synthesized pure PDPB, bare ZnO, physical mixture of PDPB and ZnO, and PDPB-ZnO NHs, was followed by the photocatalytic reduction of carcinogenic hexavalent chromium, Cr (VI) to non-toxic Cr(III) under visible light illumination as shown in Fig. 6a.

The effective removal of Cr(VI) up to 99.8% was observed in 90 min with a calculated high rate constant value of 0.015 s^{-1} (followed a pseudo-first-order reaction) using PDPB-ZnO NHs catalysts whereas ~22% reduction has been obtained for PDPB nanofibers under similar

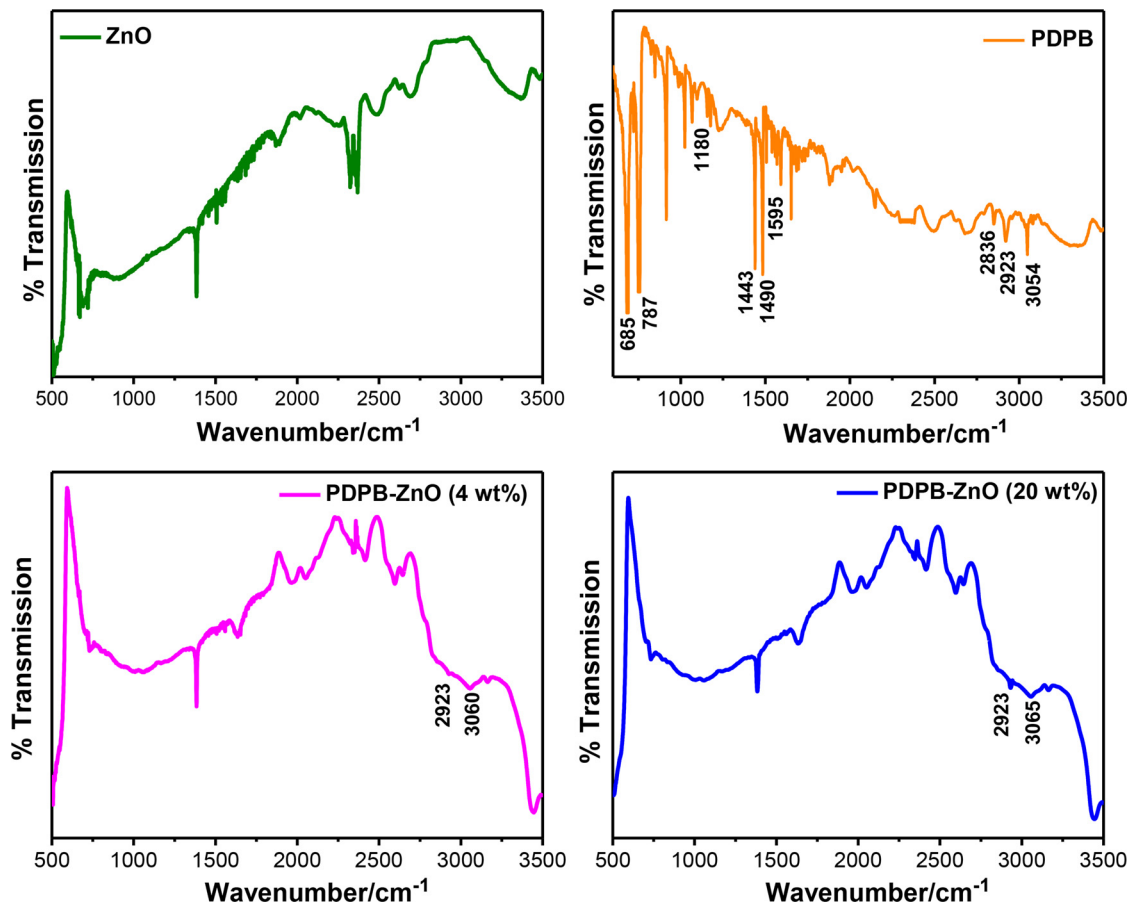


Fig. 3. FTIR spectra of ZnO (green), PDPB (orange), PDPB-ZnO (pink, 10 wt %) and PDPB-ZnO (blue, 20 wt %). (For interpretation of the references to colour in this figure legend, the reader is referred to the web version of this article.)

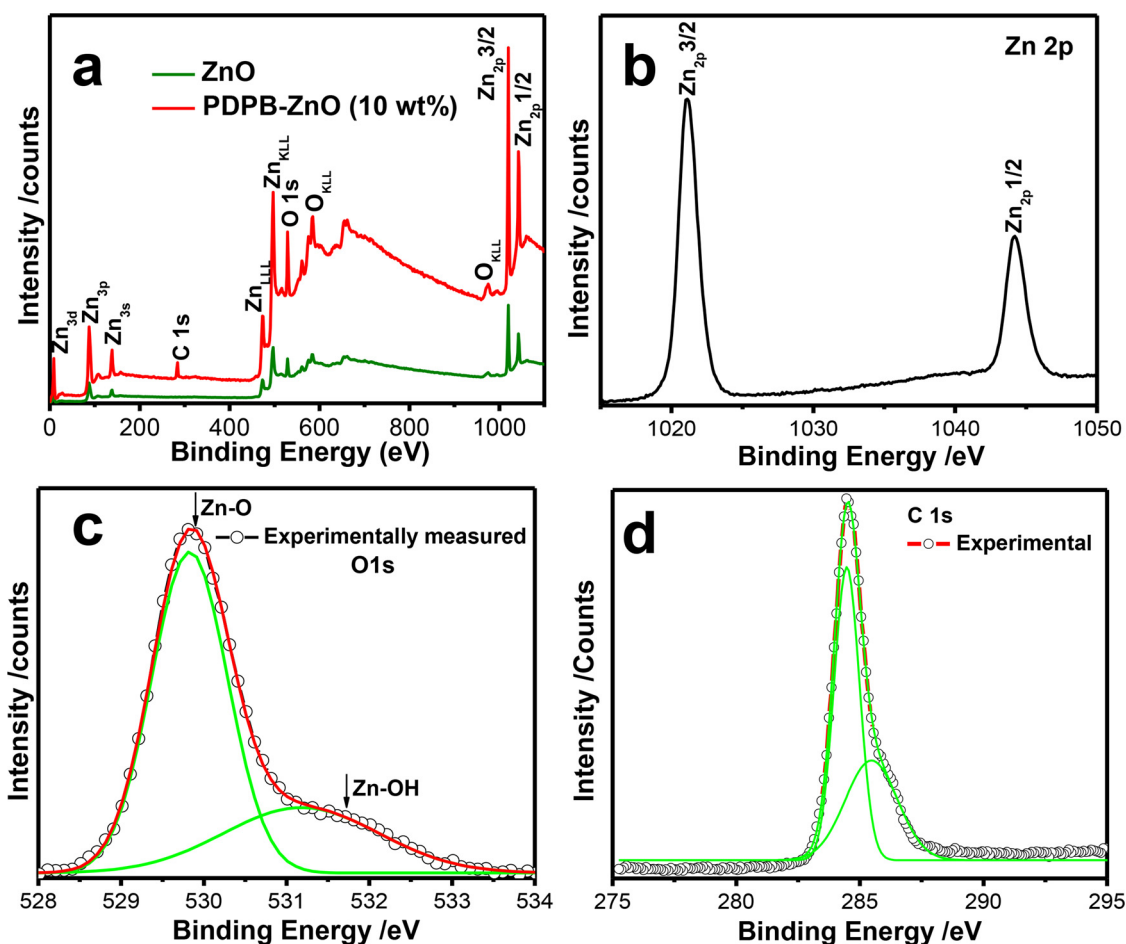


Fig. 4. (a) XPS wide survey spectra of ZnO and PDPB-ZnO nanohybrids. Core level spectra of NHs showing binding energy of (b) Zn 2p, (c) O1s and (d) C1s electrons.

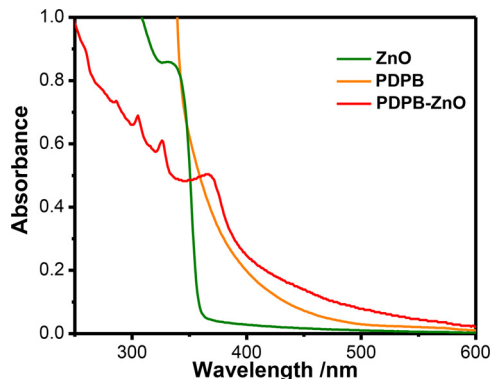


Fig. 5. UV-vis absorption spectra of ZnO (green), PDPB (orange) and PDPB-ZnO (red, 10 wt %). (For interpretation of the references to colour in this figure legend, the reader is referred to the web version of this article.)

reaction conditions. Additionally, ~28% reduction has been followed when physical mixture of PDPB and ZnO used as catalysts. The dark absorption test in the presence of the polymer and nanohybrids showed no significant change in the concentration of Cr (VI) in solution (Supplementary, Fig. S6). Fig. 6b illustrates UV – Vis absorption spectra of 50 mg/L Cr(VI) solutions treated with PDPB-ZnO NHs and the strong Cr(VI) absorptions at 255 and 355 nm decreases with time. However, no absorption of Cr(VI) at 255 and 355 nm is observed after 90 min of visible light irradiation. It is well known fact that the photocatalytic reduction of Cr (VI) at low pH is much higher than at high pH [13,14,53,54]. The photo reduction of Cr (VI) has been monitored at

different initial pH as shown in Fig. 6c. The variation of pH had an obvious influence on the reduction of chromium (VI). Higher catalytic efficiency obtain when catalytic experiments performed in acidic solutions than that in alkaline solutions. For example, 90% of reduction efficiency was achieved at pH 2 after 60 min of visible light illumination, whereas, 57% of Cr(VI) was reduced at pH 10 within the same time period. The photoreduction efficiency decreases noticeably with the increase of pH. The photo rereduction process follows pseudo first order kinetics and the rate constant (k) value decreases with increasing the pH of the working solution (from 0.015 min^{-1} at pH 2 to 0.0058 min^{-1} at pH 10, Table S1). In acidic condition, electrons can be captured by the adsorbed H^+ to form H_{ads} , which is able to reduce Cr (VI). At the same time, when increasing solution pH, Cr(III) will be precipitated on the surface of the photocatalyst as $\text{Cr}(\text{OH})_3$ and the activity sites are covered with the precipitation, so the photocatalytic activity decreases [53,54].

The initial concentration of Cr (VI) considered as an important parameter to measure the efficiency of NHs for photoreduction and removal of Cr (VI). Fig. 6d shows Cr (VI) is reduced completely in 90 min. at varied concentrations of chromium (VI) 10, 20, 50, 100, 200 mg/L, however, kinetics decreases with further increasing the concentration of Cr (VI) up to 300 mg/L at a fixed amount of catalysts concentration (rate constant decreases from 0.028 min^{-1} to 0.0074 min^{-1} at 10 mg/L and 300 mg/L Cr (VI) respectively, Table S2). This suggests the available active sites of PDPB-ZnO NHs (0.5 mg/L of 10 wt% PDPB-ZnO) could be suitable for complete removal of Cr (VI) at a concentration upto 200 mg/L. Moreover, effect of polymer loading (1–50 wt% of PDPB) on nanohybrids catalysts has been studied for the photoreduction of Cr (VI) at pH 2. Among the nanohybrids, 10 wt%

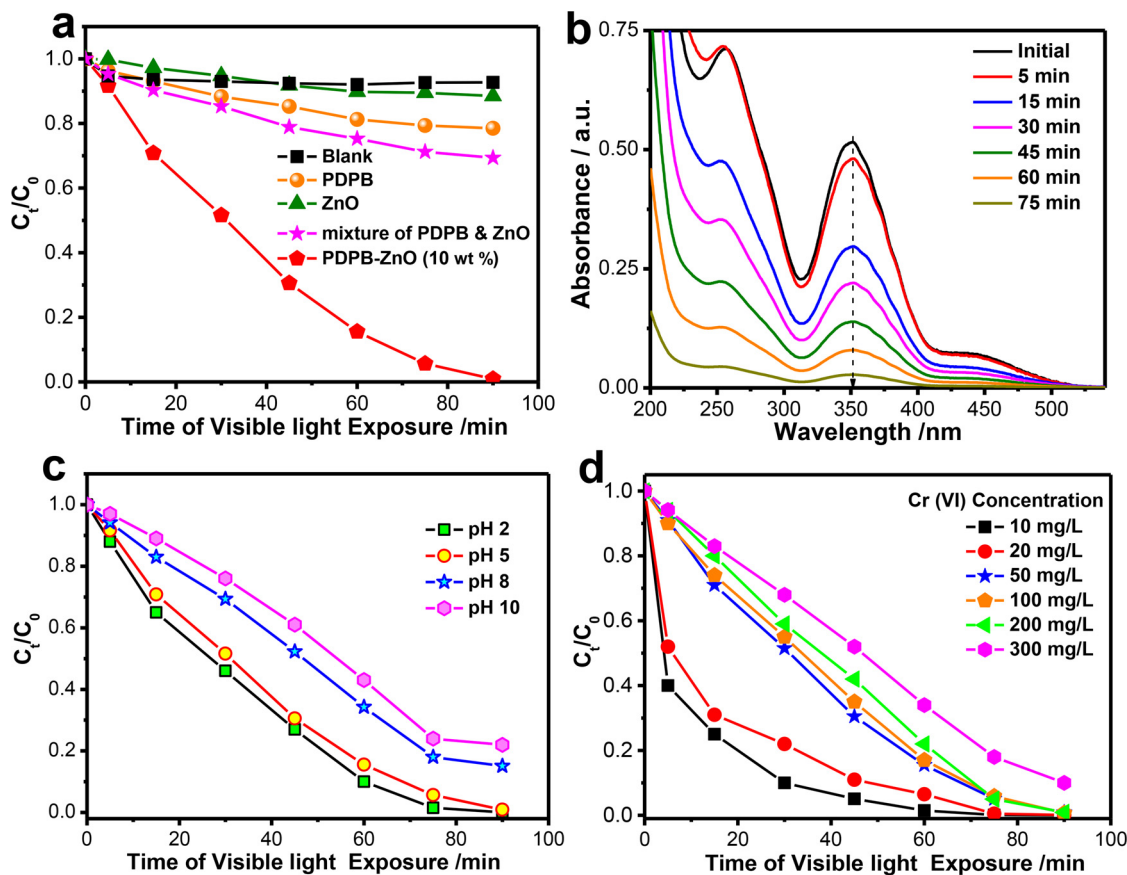


Fig. 6. (a) Photocatalytic reduction of 50 mg/L Cr(VI) solution under visible light irradiation ($\lambda \geq 450$ nm) using PDPB, ZnO, physical mixture of PDPB and ZnO, and PDPB-ZnO, as catalysts at pH 2 and blank Cr (VI) solution. (b) UV – Vis absorption spectra of Cr(VI) in the presence of the PDPB-ZnO nanohybrids. (c) Removal efficiency of 50 mg/L Cr(VI) solution at pH 2, 5, 8 and 10. (d) Effect of initial concentration of Cr(VI) on photocatalytic efficiency of PDPB-ZnO nanohybrids.

PDPB-ZnO showed the highest photocatalytic efficiency for photo-reduction of hexavalent chromium compared to 1% and 4% PDPB-ZnO, further increasing the loading of polymer (50 wt %) lowered the catalytic efficiency (Supplementary, Fig. S7).

The stability and reusability of catalysts have been considered as important aspect for large scale application. The catalytic activity of PDPB-ZnO NHs was tested through multiple cycles for the removal of Cr (VI) as shown in Fig. 7a. The photocatalytic efficiency of the recovered photocatalysts is not significantly changed more than five successive cycles (retained up to 95–98 % with its original activity). To check the stability of the NHs, XRD, TEM, and optical measurements have been carried out on the recovered PDPB-ZnO NHs. It could be clearly seen from Fig. 7b that the PDPB-ZnO NHs retained their original crystal structure even after the 7th catalytic cycle, with a slight decrease in peak intensity and no new peak has been observed which represents the stable nanostructures. Similar behaviour in optical absorbance is observed by comparing Fig. 7c with Fig. 5.

Moreover, there was no morphological change noticed in FESEM image of PDPB-ZnO NHs after cycling (Fig. 7d). This suggests that as prepared PDPB-ZnO NHs could be used several times in photocatalytic applications without compromising the quality of the particles. In order to shed light on reduction mechanism, the XPS measurement of PDPB-ZnO NHs was performed after Cr (VI) removal in Fig. 7e. All the binding energies and peak splitting of the as-synthesized sample are in good agreement with the values for recovered NHs after cycling (Supplementary, Fig. S8). Another important feature observed is the appearance of a Cr (III) species peak at 572.5 eV in the full range XPS spectrum demonstrating the photocatalytic reduction of Cr (VI) to Cr (III) as discussed in the above sections (Fig. 7e and f). While, photo reduction of Cr (VI) to Cr (III) could be possible in the presence of a reductant like

HCOOH at 45 °C using PANI/MnO₂/TiO₂ as visible light active catalysts [28]. The heterogeneous photocatalytic reduction of carcinogenic Cr (VI) using PDPB-ZnO NHs under visible light is highly efficient and economical without using any expensive noble metals, or in the absence of any strong reducing chemicals.

3.8. Mechanism

A simple mechanism has been proposed for the visible light induced Cr(VI) reduction reaction and the step by step reactions are expressed in Equation (2)–(3). As shown in Scheme 2, the band structure of the synthesized PDPB-ZnO NHs was considered in order to understand the possible process for the photocatalytic reduction of Cr(VI). When the catalysts are excited by visible light irradiation, electrons (e^-) in the valence band (VB) can be excited to the conduction band (CB) with simultaneous generation of the same amount of holes (h^+) in the VB. The excited electrons are readily injected into the conduction band of ZnO due to formation of the heterojunction, as shown in Scheme 2. After migration of these charge species to the catalysts surface, the photogenerated electrons reduce Cr (VI) to Cr(III) which is also supported by several researcher in the literature [55,56]. A visible colour change of the chromium complex solution from light yellow to colourless was observed after 90 min visible light irradiation in presence of PDPB-ZnO catalysts relating to the removal of Cr(VI). The effects of free radical scavengers on the reduction of Cr(VI) were studied to understand the reaction mechanism. The photocatalytic efficiency was higher in N₂ (99%) than in air (55%) after 90 min visible light irradiation (Supplementary, Fig. S9). The oxygen may act as an electron scavenger and contributes significantly to the photocatalytic process. As an electron scavenger, O₂ may compete with Cr(VI) for the photogenerated

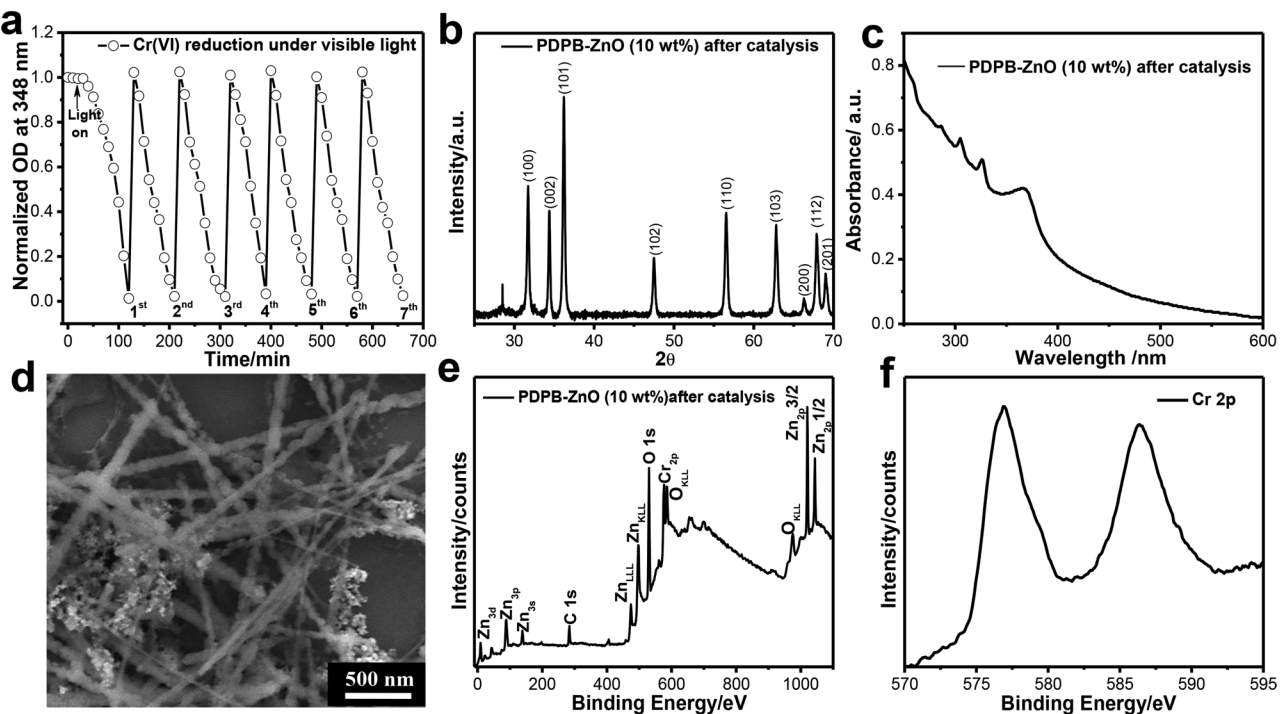
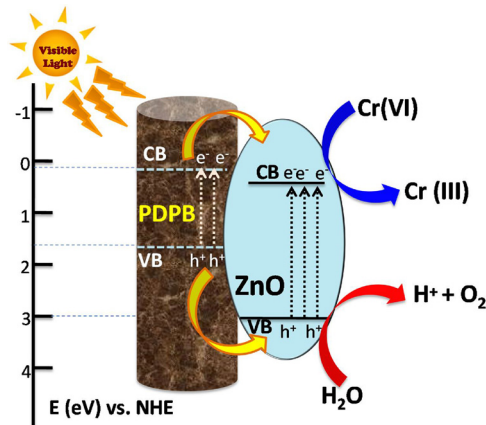
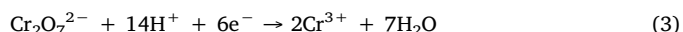
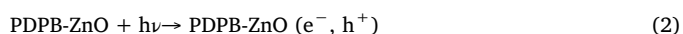


Fig. 7. Recycling and stability of the PDPB-ZnO NHs. (a) Recyclability of the PDPB-ZnO NHs photocatalysts in seven successive experiments for the photocatalytic reduction of Cr (VI) in aqueous solution under visible light irradiation. (b) XRD pattern, (c) absorption spectra and (d) FESEM image of recovered PDPB-ZnO NHs after seven cycles photocatalytic degradation of Cr(VI). XPS spectra of PDPB-ZnO nanohybrids full range (e) and enlarged (d) after seven cycle catalysis.



Scheme 2. Proposed photocatalytic process for PDPB-ZnO NHs under visible light irradiation.

electrons at CB of PDPB-ZnO catalysts, which will decrease the Cr(VI) reduction rate [57,58]. On the other hand, it is interesting to note that presence of iso-propanol as hole scavengers enhances Cr(VI) reduction (Supplementary, Fig.S9). The competitive reaction of excess holes with isopropanol lower the charge recombination rate and consequently increases the Cr(VI) reduction kinetics [32,59]. The possible mechanism of the photocatalytic reduction of hexavalent chromium at low pH is as follows (Equation 3):



The enhanced photocatalytic activities of PDPB-ZnO NHs than pure PDPB may attributed to the formation of donor-acceptor junction introduced by the n-type inorganic semiconductor (ZnO) and p-type organic semiconductor (PDPB) having higher separation and transfer efficiency of photo excited electrons. The photoluminescence (PL)

measurements also corroborate the formation of nanohybrids as evidenced from the lowering of intense visible luminescence centered ~ 520 nm (Supplementary, Fig. S10a) under the excitation wavelength of 330 nm of PDPB conjugated polymer in presence of ZnO NPs. Moreover, the interfacial charge transfer dynamics at PDPB-ZnO heterojunction suggests electrons are transferred from the conjugated polymer nanofibers to the ZnO NPs which supported with previously reported biexponential electron decay having shorter lifetime 30 ps (87%) and a longer lifetime of 1.24 ns (13%) of NHs compared to pure PDPB polymer with a rise component of 290 ps and a lifetime of 1.58 ns (monitored at 660 nm) [45].

Moreover, photocurrent measurements may provide a direct evidence of enhanced charge separation at the heterojunction interface. A steady and rapid photocurrent response is obtained from the NHs film on ITO when the irradiation is switch on and off as shown in Supplementary, Fig.S10b. Among all catalysts, PDPB-ZnO (10%) generates at least 22-fold current than bare PDPB and 2-fold higher current than PDPB-ZnO (4%), and PDPB-ZnO (20%), respectively under irradiation conditions (Supplementary, Fig.S10b). No current was produced under dark conditions, confirms the photoresponse behavior of NHs materials. The maximum photocurrent density ($15.4 \mu\text{A}/\text{cm}^2$) is obtained for thin film electrode of PDPB-ZnO (10%) which is 6 times higher than that obtained on bare ZnO thin film electrode. Thus the photocurrent for PDPB-ZnO was much higher than that of bare PDPB and pure ZnO. This indicates the effective absorption of light and efficient charge transfer due to formation of multiple heterojunctions in PDPB-ZnO (10%) which may help to achieve high current than other compositions which also corroborates the higher catalytic activity obtained from this composition. Hence, because of high photocurrent generation, PDPB-ZnO (10%) shows high photocatalytic degradation photocatalytic reduction of hexavalent chromium.

In order to understand the intrinsic electronic properties, the energy band structure including band gaps, conduction band (CB) and valence band (VB) positions of ZnO, PDPB, PDPB-ZnO NHs, Mott-Schottky (M-S) analysis ($1/C^2$ versus electrode potential) has been performed. The flat band potential of a semiconductor can be obtained from Mott-

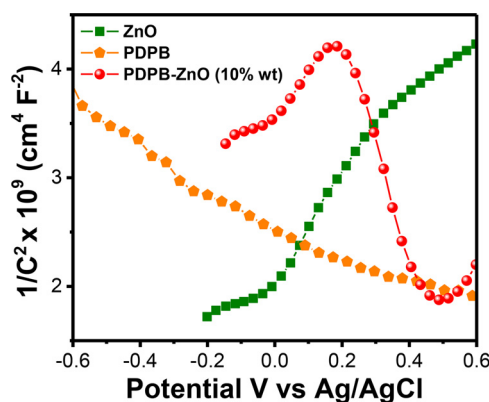


Fig. 8. Mott-Schottky plots for pure ZnO, PDPB and PDPB-ZnO NHs (10%) in the presence of 0.1 M Na_2SO_4 electrolytes (pH 7) using an AC frequency of 1000 Hz. The intercept of the plot (at $1/C^2 = 0$) has been used to determine the V_{FB} of the ZnO, PDPB and PDPB-ZnO NHs photoelectrodes.

Schottky plot using the Equation 4:

$$\frac{1}{C^2} = \frac{2}{q\epsilon\epsilon_0 N_d} (V_{app} - V_{FB} - \frac{kT}{q}) \quad (4)$$

Where, ϵ is the dielectric constant of the semiconductor, ϵ_0 is the permittivity of the vacuum, N_d is the donor density, V_{app} is the applied potential, V_{FB} is the flat band potential and kT/q is the temperature-dependent term. The intercept of linear plot at $1/C^2 = 0$ gives the flat band potential.

In Fig. 8, the ZnO shows a negative slope in the M-S plots with flat band potential -0.34 V (vs Ag/AgCl), indicating n-type behavior with electrons as the majority carriers. In contrast, PDPB shows a positive slope in the M-S plots with flat band potential 1.61 V (vs Ag/AgCl), indicating p-type behavior. However, the co-existence of positive and negative slopes with two flat band potential values (-0.88 V and 0.68 V vs. Ag/AgCl) have been observed for PDPB-ZnO NHs (10%), indicating the formation of p-n junction within the nanohybrids (Supplementary, Table S3). The flat band potential of PDPB-ZnO NHs is more negative when compare to pure ZnO, suggesting the decrease in band bending, consequently facilitating the transfer of electrons. Moreover, the charge carrier concentration (N_d) can be calculated from the slope of M-S plot. The N_d values for ZnO, PDPB, and PDPB-ZnO NHs are estimated as 2.5×10^{19} cm^{-3} , 6.2×10^{19} and 8.5×10^{19} cm^{-3} respectively. An increase in the N_d value suggests that charge transfer of ZnO has been improved due to formation of heterojunction with conducting polymer, which facilitates the charge separation.

3.9. Photoelectrochemical (PEC) activity

The photoelectrochemical (PEC) measurement have been followed through the linear-sweep-voltammetry (LSV) technique for bare PDPB, ZnO, and PDPB-ZnO NHs using a three electrode photoelectrochemical cell in 0.1 M Na_2SO_4 solution both under dark condition and under light illumination (Fig. 9a and 9b). The measured photocurrent was normalized with the sample area to obtain the photocurrent density. The current density in the dark remained at a very low level from -1.0 to 0.8 V [vs. Ag/AgCl], but a prompt photocurrent increase appeared after illumination with visible light. The photocurrent density value of the PDPB-ZnO electrode is significantly higher than that of the bare PDPB and ZnO electrode. As presented in Fig. 9a, the PDPB-ZnO electrode produce a photocurrent density of 5.7×10^{-4} A cm^{-2} at potential of 0.8 V vs. Ag/AgCl which is 8.1 times higher than PDPB electrodes (7×10^{-5} A cm^{-2} , Fig. 9b). The low photocurrent density is attributed to the limit of wide band-gap characteristics of ZnO (3.39 eV), due to which only UV light can be used in the PEC water splitting system (Fig. 9c).

The stability of the all electrode has been followed by chronamperometric measurement under continuous illumination (Fig. 9d-f). The photocurrent density is decreases from 4.8×10^{-4} A cm^{-2} to 4×10^{-4} A cm^{-2} for PDPB-ZnO electrode as shown in Fig. 9d. While, for PDPB electrode, the photocurrent density drops about 22% (4.4×10^{-5} A cm^{-2} to 3.1×10^{-5} A cm^{-2}) after 300 min. as shown in Fig. 9e. This may associated with photo induced corrosion which competes with water oxidation reaction. Such photo corrosion of PDPB nanofibers could be suppressed by surface modification with ZnO NPs for long term application. While bare ZnO also showed significant photocurrent loss upto 80% after 300 min. under similar reaction condition (Fig. 9f) due to fast recombination rate of photogenerated charge carrier.

Electrochemical impedance spectroscopy (EIS) has been used to probe charge transfer properties at the electrode/solution interface. Fig. 10 shows the EIS Nyquist plots of PDPB nanofibers and PDPB-ZnO NHs where the semicircle portion corresponds to the charge transfer process, with the diameter of the semicircle equivalent to the charge transfer resistance (R_{ct}). While the linear portion reflects the diffusion limited processes at the electrode interface. The charge transfer resistance (R_{ct}) decreased from 107.7Ω (PDPB) to 21.5Ω (PDPB-ZnO), suggesting that the PDPB-ZnO NHs can facilitate the charge transfer.

The inset in Fig. 10 shows Randles equivalent circuit model for EIS analysis. The total electrode impedance corresponds to the electron transfer resistance (R_{ct}) in series with the parallel connection of the double layer capacitance (C_{dl}) and Warburg impedance (Z_w) [60]. Hence, EIS results suggested that presence of ZnO nanoparticles in nanohybrid could significantly improve the electron transfer efficiency of conducting polymer and the photocatalytic efficiency.

4. Conclusions

In summary, PDPB-ZnO nanohybrids have been developed by a facile adsorption of ZnO NPs on conducting polymer nanofibers in absence of any harsh reducing and oxidizing species for photocatalytic applications. The as-prepared PDPB-ZnO nanohybrids demonstrated superior photocatalytic activity for the reduction of poisonous Cr(VI) to environmentally benign Cr (III) under visible light irradiation without incorporation of any expensive noble metals and hence useful for large scale application. The removal efficiency of Cr (VI) is extremely higher (99.5%) in acidic solutions at pH 2 than that in alkaline solution pH 10, where 77% of Cr (VI) was reduced at within the same time period. The PEC performance test reveals that the photocurrent of PDPB-ZnO is 8.1 times greater than that of the PDPB photoelectrode. The excellent photocatalytic activity of nanohybrids can be obtained from the co-sensitization of ZnO NPs by oligomeric and polymer chain unit of polymer nanofibers and efficient charge separation of photogenerated charge carriers. The enhanced charge separation at the polymer-metal oxides interface was also supported by interfacial carrier dynamics by detailed steady state and ultrafast spectroscopic studies. Mott-Schottky and impedance analysis confirm effective charge separation at the interfaces of heterojunction which lead to enhance the photocurrent generation and catalytic activity of PDPB-ZnO nanohybrids compared to the bare ZnO. Notably, the PDPB-ZnO nanohybrids can be easily reused for more than six cycles for photoreduction of Cr (VI) and retain their original morphology, crystal structure and optical properties in recovered catalysts. Hence, PDPB-ZnO nanohybrid can be utilized as visible light active photocatalysts for large scale application. Solar conversion at the polymer-semiconductor interface overcomes the high activation barrier of excitons in pure polymers as well as small spectral overlap of semiconductor nanostructures with the broad solar spectrum of polymer due to the synergistic advantages of both components.

Acknowledgements

The authors acknowledge Director, CSIR-CGCRI for his kind

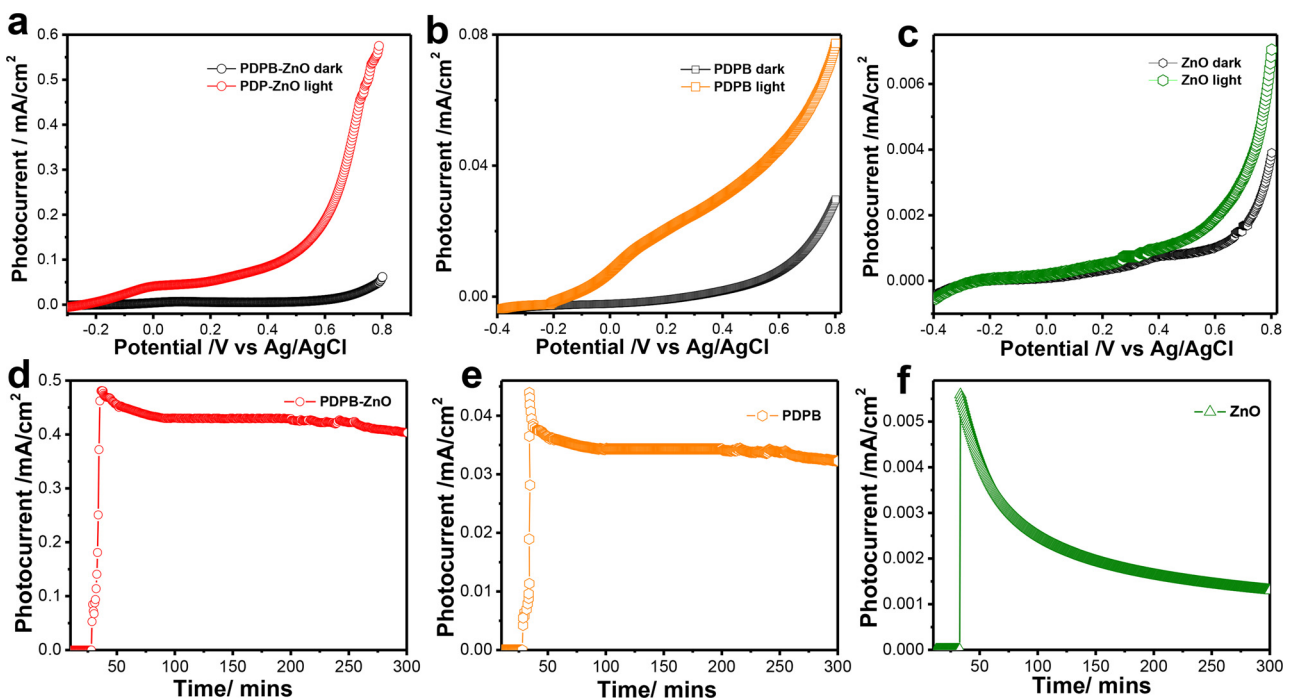


Fig. 9. Photoelectrochemical current density vs potential plot of (a) PDPB-ZnO NHs, (b) PDPB and (c) ZnO using LSV method under dark and light illumination with output intensity 100 mW cm^{-2} at a scan rate 20 mV sec^{-1} using $0.1 \text{ M Na}_2\text{SO}_4$ solution as electrolyte, Pt wire as counter electrode and Ag/AgCl as reference electrode. Time dependence photocurrent density at external bias 0.26 V vs Ag/AgCl with illumination, at scan rate 20 mV sec^{-1} for (d) PDPB-ZnO NHs, (e) PDPB, and (f) ZnO.

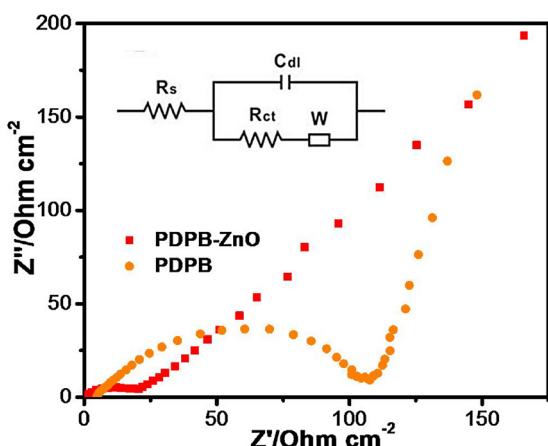


Fig. 10. The electrochemical impedance of (a) PDPB-ZnO NHs (b) bare PDPB in $0.1 \text{ M Na}_2\text{SO}_4$ aqueous solution. Inset: Randles equivalent circuit model.

permission to publish the work. One of the authors (SG) is thankful to Council of Scientific & Industrial Research (CSIR), India, for providing CSIR-Senior Research Associateship (Scientists' Pool Scheme).

Appendix A. Supplementary data

Supplementary material related to this article can be found, in the online version, at doi:<https://doi.org/10.1016/j.apcatb.2018.08.034>.

References

- [1] A. Kubacka, M.F. Garcia, G. Colon, Chem. Rev. 112 (2012) 1555–1614.
- [2] S. Ghosh (Ed.), Visible-Light-Active Photocatalysis: Nanostructured Catalyst Design, Mechanisms, and Application, Wiley-VCH VerlagGmbH & Co, KGaA, 2018ISBN: 978-3-527-34293-8.
- [3] S.Y. Tee, K.Y. Win, W.S. Teo, L.-D. Koh, S. Liu, C.P. Teng, M.-Y. Han, Adv. Sci. 4 (2017) 1–24 1600337.
- [4] C. Jiang, S.J.A. Moniz, A. Wang, T. Zhang, J. Tang, Chem. Soc. Rev. 46 (2017) 4645–4660.
- [5] I. Roger, M.A. Shipman, M.D. Symes, Nat. Rev. Chem. 1 (2017) 0003.
- [6] T. Hisatomi, J. Kubota, K. Domen, Chem. Soc. Rev. 43 (2014) 7520–7535.
- [7] P. Pichat (Ed.), Photocatalysis and Water Purification: From Fundamentals to Recent Applications, Wiley-VCH Verlag GmbH & Co, KGaA, 2013ISBN: 9783527331871.
- [8] T.C. Machado, M.A. Lansarin, N. Matte, Water Sci. Technol. 70 (2014) 55–61.
- [9] WHO, Chromium in Drinking-water. Background Document for Preparation of WHO Guidelines for Drinking-water Quality, Word Health Organization, Geneva, 2003.
- [10] M. Chebeir, G. Chen, H. Liu, Environ. Sci. Water Res. Technol. 2 (2016) 906–914.
- [11] R. Mehra, M. Juneja, Indian J. Biochem. Biophys. 40 (2003) 131–135.
- [12] L.C. Cid, Md.C. Grande, E.O. Acosta, B. Ginzberg, Ind. Eng. Chem. Res. 51 (2012) 9468–9474.
- [13] J.M. Meichtry, C. Colbeau-Justin, G. Custo, M.I. Litter, Catal. Today 224 (2014) 236–243.
- [14] V.N. Montesinos, C. Salou, J.M. Meichtry, C. Colbeau-Justin, M.I. Litter, Photochem. Photobiol. Sci. 15 (2016) 228–234.
- [15] M.S. Siboni, M. Farrokhi, R.D.C. Soltani, A. Khataee, S. Tajassosi, Ind. Eng. Chem. Res. 53 (2014) 1079–1087.
- [16] P. Banerjee, S. Chakrabarti, S. Maitra, B.K. Dutta, Ultrason. Sonochem. 19 (2012) 85–93.
- [17] M.G. Méndez-Medrano, E. Kowalska, A. Lehoux, A. Herissan, B. Ohtani, D. Bahena, V. Brioso, C. Colbeau-Justin, J.L. Rodriguez-López, H. Remita, J. Phys. Chem. C 120 (2016) 5143–5154.
- [18] A.L. Luna, E. Novoseltceva, E. Louarn, P. Beaunier, E. Kowalska, B. Ohtani, M.A. Valenzuela, H. Remita, C. Colbeau-Justin, Appl. Catal. B: Environ. 191 (2016) 18–28.
- [19] H. Park, H.-il Kim, G.-h. Moon, W. Choi, Energy Environ. Sci. 9 (2016) 411–433.
- [20] J. Kuncewicz, P. Ząbek, K. Kruczak, K. Szaciłowski, W. Macyk, J. Phys. Chem. C 116 (2012) 21762–21770.
- [21] S. Luo, Y. Xiao, L. Yang, C. Liu, F. Su, Y. Li, Q. Cai, G. Zeng, Sep. Purif. Technol. 79 (2011) 85–91.
- [22] J.W. Su, Y.X. Zhang, S.C. Xu, S. Wang, H.L. Ding, S.S. Pan, G.Z. Wang, G.H. Li, H.J. Zhao, Nanoscale 6 (2014) 5181–5192.
- [23] Y.C. Zhang, J. Li, M. Zhang, D.-D. Dionysiou, Environ. Sci. Technol. 45 (2011) 9324–9331.
- [24] C. Mondal, M. Ganguly, J. Pal, A. Roy, J. Jana, T. Pal, Langmuir 30 (2014) 4157–4164.
- [25] P. Kush, K. Deori, A. Kumar, S. Deka, J. Mater. Chem. A 3 (2015) 8098–8106.
- [26] Y. Zhong, X. Qiu, D. Chen, N. Li, Q. Xu, H. Li, J. He, J. Lu, ACS Appl. Mater. Interfaces 8 (2016) 28671–28677.
- [27] B. Vellaichamy, P. Periakaruppan, B. Nagulan, ACS Sustainable Chem. Eng. 5 (2017) 9313–9324.

[28] D.K. Padhi, A. Baral, K. Parida, S.K. Singh, M.K. Ghosh, *J. Phys. Chem. C* 121 (2017) 6039–6049.

[29] D.K. Padhi, T.K. Panigrahi, K. Parida, S.K. Singh, P.M. Mishra, *ACS Sustainable Chem. Eng.* 5 (2017) 10551–10562.

[30] J.M. Meichtry, V. Rivera, Y.D. Iorio, H.B. Rodríguez, E. San Román, M.A. Grela, M.I. Litter, *Photochem. Photobiol. Sci.* 8 (2009) 604–612.

[31] S. Ghosh, M. Thandavaray, R.N. Basu, *Nanoscale* 8 (2016) 6921–6947.

[32] S. Ghosh, N.A. Kouame, L. Ramos, S. Remita, A. Dazzi, A. Deniset-Besseau, P. Beaunier, F. Goubard, P.-H. Aubert, H. Remita, *Nat. Mater.* 14 (2015) 505–511.

[33] S. Ghosh, N.A. Kouamé, S. Remita, L. Ramos, F. Goubard, P.-H. Aubert, A. Dazzi, A. Deniset-Besseau, H. Remita, *Sci. Rep.* 5 (2015) 18002–18011.

[34] D. Floresyona, F. Goubard, P.-H. Aubert, I. Lampre, J. Mathurin, A. Dazzi, S. Ghosh, P. Beaunier, F. Brisset, S. Remita, L. Ramos, H. Remita, *Appl. Catal. B: Environ.* 209 (2017) 23–32.

[35] S. Ghosh, L. Ramos, H. Remita, *Nanoscale* 10 (2018) 5793–5819.

[36] C. Su, R. Tandiana, B. Tian, A. Sengupta, W. Tang, J. Su, K.P. Loh, *ACS Catal.* 6 (2016) 3594–3599.

[37] J. Liu, Y. Liu, N. Liu, Y. Han, X. Zhang, H. Huang, Y. Lifshitz, S.-T. Lee, J. Zhong, Z. Kang, *Science* 347 (2015) 970–974.

[38] L. Wang, Y. Wan, Y. Ding, S. Wu, Y. Zhang, X. Zhang, G. Zhang, Y. Xiong, X. Wu, J. Yang, H. Xu, *Adv. Mater.* 29 (2017) 1–8 1702428.

[39] J. Belloni, M. Tréguer, H. Remita, R.D. Keyser, *Nature* 402 (1999) 865–867.

[40] P. Reiss, E. Couderc, J. Girolamo, A. Pron, *Nanoscale* 3 (2011) 446–489.

[41] Y.W. Su, W.H. Lin, Y.J. Hsu, K.H. Wei, *Small* 10 (2014) 4427–4442.

[42] S. Ghosh, A.K. Mallik, R.N. Basu, *Sol. Energy* 159 (2018) 548–560.

[43] Y. Wang, Y. Deng, L. Fan, Y. Zhao, B. Shen, D. Wu, Y. Zhou, C. Dong, M. Xing, J. Zhang, *RSC Adv.* 7 (2017) 24064–24069.

[44] J. Lei, F. Liu, L. Wang, Y. Liu, J. Zhang, *RSC Adv.* 7 (2017) 27377–27383.

[45] S. Sardar, P. Kar, H. Remita, B. Liu, P. Lemmens, S.K. Pal, S. Ghosh, *Sci. Rep.* 5 (2015) 17313–17327.

[46] S. Ghosh, H. Remita, L. Ramos, A. Dazzi, A. Deniset-Besseau, P. Beaunier, F. Goubard, P.-H. Aubert, F. Brisset, S. Remita, *New J. Chem.* 38 (2014) 1106–1115.

[47] S. Hayashi, N. Nakamori, H. Kanamori, *J. Phys. Soc. Japan* 46 (1979) 176–183.

[48] S.A. Ansari, M.M. Khan, S. Kalathil, A. Nisar, J. Lee, M.H. Cho, *Nanoscale* 5 (2013) 9238–9246.

[49] R. Al-Gaashania, S. Radimana, A.R. Dauda, N. Tabetc, Y. Al-Dourid, *Ceram. Int.* 39 (2013) 2283–2292.

[50] J. Das, S.K. Pradhan, D.R. Sahu, D.K. Mishra, S.N. Sarangi, B.B. Nayak, S. Verma, B.K. Roul, *Physica B* 405 (2010) 2492–2497.

[51] H. Zhou, Z. Li, *Mater. Chem. Phys.* 89 (2005) 326–331.

[52] W.H. Lee, S.J. Kim, W.J. Lee, J.G. Lee, R.C. Haddon, P.J. Reucroft, *Appl. Surf. Sci.* 181 (2001) 121–127.

[53] K. Bhowmik, A. Mukherjee, M.K. Mishra, G. De, *Langmuir* 30 (2014) 3209–3216.

[54] L.B. Khalil, W.E. Mourad, M.W. Rophael, *Appl. Catal. B: Environ.* 17 (1998) 267–273.

[55] P. Mohapatra, S.K. Samantaray, K. Parida, J. *Photochem. Photobiol. A Chem.* 170 (2005) 189–194.

[56] J.A. Navío, G. Colom, M. Trillas, J. Peral, X. Domenech, J.J. Testa, J. Padron, D. Rodríguez, M.I. Litter, *Appl. Catal. B: Environ.* 16 (1998) 187–196.

[57] M.Q. Wu, J. Zhao, G. Qin, C. Wang, X. Tong, S. Xu, *Appl. Catal. B: Environ.* 142–143 (2013) 142–148.

[58] A. Hérisson, J.M. Meichtry, H. Remita, C. Colbeau-Justin, M.I. Litter, *Catal. Today* 281 (2017) 101–108.

[59] J.J. Testa, M.A.A. Grela, M.I. Litter, *Environ. Sci. Technol.* 38 (2004) 1589–1594.

[60] B. Klahr, S. Gimenez, F. Fabregat-Santiago, T. Hamann, J. Bisquert, *J. Am. Chem. Soc.* 134 (2012) 4294–4302.